

Evidences for pressure-induced two-phase superconductivity and mixed structures of NiTe₂ and NiTe in type-II Dirac semimetal NiTe_{2-x} ($x = 0.38 \pm 0.09$) single crystals



Z. Feng^{a,**}, J. Si^a, T. Li^a, H. Dong^b, C. Xu^c, J. Yang^a, Z. Zhang^a, K. Wang^{a,b}, H. Wu^{a,b}, Q. Hou^a, J.-J. Xing^a, S. Wan^b, S. Li^b, W. Deng^b, J. Feng^b, A. Pal^a, F. Chen^a, S. Hu^a, J.-Y. Ge^a, C. Dong^d, S. Wang^a, W. Ren^e, S. Cao^{a,e}, Y. Liu^f, X. Xu^f, J. Zhang^{a,****}, B. Chen^{b,***}, N.-C. Yeh^{g,*}

HPSTAR
1118-2021

^a Materials Genome Institute, Shanghai University, Shanghai, 200444, China

^b Center for High Pressure Science and Technology Advanced Research, Shanghai, 201203, China

^c School of Physics and Key Laboratory of MEMS of the Ministry of Education, Southeast University, Nanjing, 211189, China

^d School of Advanced Materials, Peking University Shenzhen Graduate School, Shenzhen, 518055, Guangdong, China

^e Shanghai Key Laboratory of High Temperature Superconductors, Department of Physics, Shanghai University, Shanghai, 200444, China

^f Department of Applied Physics, Zhejiang University of Technology, Hangzhou, 310023, China

^g Department of Physics, California Institute of Technology, Pasadena, CA, 91125, USA

ARTICLE INFO

Article history:

Received 5 December 2020

Received in revised form

27 December 2020

Accepted 30 December 2020

Available online 18 January 2021

Keywords:

NiTe_{2-x}

Multi-band superconductivity

Single-band superconductivity

Type-II Dirac Semimetal

ABSTRACT

Bulk NiTe₂ is a type-II Dirac semimetal with non-trivial Berry phases associated with the Dirac fermions. Theory suggests that monolayer NiTe₂ is a two-gap superconductor, whereas experimental investigation of bulk NiTe_{1.98} for pressures (P) up to 71.2 GPa do not reveal any superconductivity. Here we report experimental evidences for pressure-induced two-phase superconductivity as well as mixed structures of NiTe₂ and NiTe in Te-deficient NiTe_{2-x} ($x = 0.38 \pm 0.09$) single crystals. Hole-dominant multi-band superconductivity with the $P\bar{3}m1$ hexagonal-symmetry structure of NiTe₂ appears at $P \geq 0.5$ GPa, whereas electron-dominant single-band superconductivity with the $P2/m$ monoclinic-symmetry structure of NiTe emerges at 14.5 GPa $< P < 18.4$ GPa. The coexistence of hexagonal and monoclinic structures and two-phase superconductivity is accompanied by a zero Hall coefficient up to ~ 40 GPa, and the second superconducting phase prevails above 40 GPa, reaching a maximum $T_c = 7.8$ K and persisting up to 52.8 GPa. Our findings suggest the critical role of Te-vacancies in the occurrence of superconductivity and potentially nontrivial topological properties in NiTe_{2-x}.

© 2020 Elsevier Ltd. All rights reserved.

1. Introduction

Transition metal dichalcogenides (TMDs) MX₂ ($M = \text{Mo, W, Zr, Pt, Pd, Ni, Nb}$; $X = \text{S, Se, Te}$) have attracted intense research interest because of their rich physical properties, ranging from strong spin-valley coupling in monolayer 2H-phase TMDs [1,2], direction-dependent chiral anomaly and novel quantum oscillations in

type-II Dirac/Weyl semimetals [3,4], to exotic superconductivity in some 2H-phase and 1T/1T'-phase TMDs [5–10]. Among the superconducting TMDs, 2H-phase NbS₂, NbSe₂, MoS₂, MoSe₂ and TaS₂ reveal novel Ising superconductivity even in the monolayer limit [5,7]. In the case of 1T'-phase superconducting TMDs such as MoTe₂ and WTe₂, the non-trivial Berry phases and topological surface states of these type-II Weyl semimetals are promising ingredients for topological superconductors [8–10]. However, the superconducting transition temperatures (T_c) of both MoTe₂ and WTe₂ are very low (< 0.1 K) [8–10], so that various approaches have been explored to enhance the superconductivity, including partially replacing Te in MoTe₂ with either S or Se [11,12], applying pressure to MoTe₂ [8], WTe₂ [9,10] and Mo_{1-x}W_xTe₂ [13], and intercalating potassium into WTe₂ [14]. Similarly, intercalation of

* Corresponding author.

** Corresponding author.

*** Corresponding author.

**** Corresponding author.

E-mail addresses: fengzhenjie@shu.edu.cn (Z. Feng), jczhang@shu.edu.cn (J. Zhang), chenbin@hpstar.ac.cn (B. Chen), ncyeh@caltech.edu (N.-C. Yeh).

Cu into ZrTe₂ is found to induce multi-band superconductivity [15]. Other widely studied type-II Dirac/Weyl semimetals include PtTe₂ and PdTe₂ [16,17], although no direct experimental evidence for superconductivity has been reported in these systems.

The NiTe₂ system, a type-II Dirac semimetal [18,19], has recently received significant attention because of the observation of various novel phenomena, including linear field dependence of magnetoresistance due to the contribution of Dirac fermions with a Fermi level (E_F) near the Dirac nodes [20,21], and the planar Hall effect due to orbital magnetoresistance [22]. Additionally, theoretical studies have predicted two-gap superconductivity with $T_c \sim 5.7$ K in monolayer NiTe₂ and absence of superconductivity in bulk NiTe₂ [23]. These interesting findings suggest that NiTe₂ is a TMD system worthy of further investigation. Moreover, recent reports of pressure-induced superconductivity in a variety of topological materials [24–27] have motivated the exploration of possible pressure-induced topological superconductivity in NiTe₂. However, experimental studies of nearly stoichiometric NiTe_{1.98} single crystals under pressures (P) up to 71.2 GPa have found steady increase in resistivity with pressure without any hints of superconductivity [28], except that an electronic topological transition (also known as the Lifshitz transition) at $P_c \sim 16$ GPa was proposed [28].

Here we report experimental evidences for pressure-induced superconductivity in non-stoichiometric NiTe_{2-x} ($x = 0.38 \pm 0.09$) single crystals. In addition to the finding of two superconducting phases, the normal-state properties of Te-deficient NiTe_{2-x} exhibit significant differences from those found in NiTe₂, and the two pressure-dependent superconducting phases are correlated with two different crystalline structures. One is a hexagonal (NiTe₂ + Te-vacancies) $P\bar{3}m1$ phase (H-phase), and the other is a monoclinic P2/m phase (M-phase NiTe), which emerges at ~ 16 GPa where a Lifshitz transition was found in NiTe_{1.98} [28]. Our studies of various pressure-dependent properties suggest that Te-vacancies in NiTe_{2-x} play an important role in the structural and electronic properties as well as the appearance of two-phase superconductivity, and that the wide pressure range for a charge-compensated state with a vanishing Hall coefficient is promising for further investigation of topological superconductivity.

2. Materials and methods

2.1. Synthesis

Single crystalline NiTe_{2-x} ($0.3 < x < 0.5$) samples were synthesized in Te solution. Accurately weighed amounts of high purity nickel powder and tellurium ingots were mixed thoroughly with a molar ratio of 1:8 in a glovebox and then sealed in an evacuated quartz tube. This quartz tube was then heated to 950 °C quickly in a sintering furnace and kept at this temperature for 48 h, before being slowly cooled down to (550 ± 20) °C at a rate of 3 °C/h, and finally quenched in cold water. The excess amount of Te was centrifuged at 500 °C. The air stable, large pieces of dark-gray layered single crystals of NiTe_{2-x} of typical 7–8 mm in length were harvested.

2.2. Determining the chemical composition of NiTe_{2-x}

The Ni-to-Te atomic ratios of the single crystalline samples were determined by the energy dispersive X-ray spectrum (EDS) using two different scanning electron microscopes, one was SU 5000 (Hitachi, Japan), and the other was Gemini SEM 300 (Carl Zeiss, Germany). The EDS studies are detailed in Supplementary Information (Figures S2–S5).

2.3. Structural characterization at ambient pressure

To investigate the ambient-pressure structures of NiTe_{2-x} single crystals, some of the single crystals were grinded into powder and then studied using the powder X-ray diffraction (XRD) data on Bruker D8 Discovery. Powder XRD patterns confirmed a pure trigonal phase with the $P\bar{3}m1$ symmetry. The Rietveld refinement was carried out by GSAS-II software [29] and the lattice parameters were determined to be $a = 3.8553$ Å and $c = 5.2630$ Å, which were smaller than previously reported values of $a = 3.8776$ Å and $c = 5.2653$ Å for stoichiometric NiTe_{1.98} [28].

2.4. Pressure dependent structural characterization

Some of the single crystals were grinded into powder and then room temperature pressure-dependent figures of powder diffraction rings were obtained at BL15U1 (20 Kev) beamline of the SSRF with a wavelength = 0.6199 Å. The pressure transmission medium for the high-pressure X-ray measurements was silicon oil. The diffraction rings were then integrated into powder diffraction patterns using the Dioptas software [30]. Subsequently, the evolution of the pressure-dependent crystal structures and lattice parameters were analyzed, indexed, and refined by EXPO2014 [31], Fullprof Suit [32], VESTA [33] and GSAS-II [29] software.

2.5. Pressure dependent electrical transport measurements

The electrical resistivity was measured with a standard four-terminal method covering a temperature range from 2 to 300 K with the incorporation of a diamond anvil cell in a Physical Property Measurement System (PPMS-14, Quantum Design, Inc.). The material of the diamond anvil cell and the gasket was Cu–Be alloy. The diameter of the culet was 300 μm and the typical sample size was about 80 μm × 60 μm. The pressure was determined by measuring the position of fluorescence lines of ruby. Typical current densities used for the resistive measurements were ~ 100 A/m². No apparent dependence on the current density was found up to ~ 2000 A/m², whereas resistive signals became difficult to resolve for current densities significantly smaller than 100 A/m².

2.6. Pressure-dependent Raman spectroscopic measurements

A Renishaw inVia microscope was employed to obtain Raman spectra data using a 633 nm continuous wave mode laser with 1800 optical grating. The exposure time for one scan was 60 s; 3 scans were performed and integrated together for one sample to improve the signal-noise ratio. NaCl soft powder was used as the pressure transmission medium, which was consistent with the transmission medium used in the pressure dependent electrical transport measurements.

3. Density functional theory calculations

We carried out calculations of the density of states (DOS) by using density functional theory (DFT) within the Perdew–Burke–Ernzerhof generalized gradient approximation, as implemented in the Vienna *ab initio* simulation package [34,35]. The projector augmented wave method was adopted [36]. The planewave cutoff energy was set to be 360 eV. NiTe and NiTe₂ were calculated in their unit cells, while NiTe_{1.625} was calculated in a supercell of Ni₆₄Te₁₀₄. The Te/vacancy ordering in NiTe_{1.625} was constructed by using the special quasi-random structure method [37]. The lattice parameters of all the structures were taken from our experiments, and the atomic positions were fully relaxed. The energy and force

convergence criteria for all the structures were 10^{-4} eV and 10^{-2} eV/Å, respectively. We further note that our calculations had assumed an independent, stable NiTe structure, although in reality this pressure-induced M-phase in NiTe_{2-x} was not a stable structure on its own and could only coexist with the H-phase. How the interplay of these interconnected phases affected the electronic properties and superconductivity of NiTe_{2-x} had not been explicitly considered.

4. Results

4.1. Structural and compositional characterizations

The synthesis procedures for NiTe_{2-x} single crystals were mostly consistent with previous work [20] as summarized in Subsection 2.1, except that the final temperature for our sample growth before quenching the samples into cold water was a few tens of degrees higher. The Rietveld refinement results of the ambient-pressure structure is shown in Figure S1. The chemical composition of the single crystals was analyzed using Energy Dispersive X-ray Spectroscopy (EDS) on a set of crystals with multiple spots on each, as described in Subsection 2.2. The Ni-to-Te atomic ratio for different crystals at different sample areas ranged from 1.53 to 1.71 so that $x = 0.38 \pm 0.09$ for NiTe_{2-x} (Figures S2-S5), with microscopically uniform distributions of Te-vacancies throughout each single crystal (Figure S5).

The structural properties and pressure-dependent lattice constants of single crystalline NiTe_{2-x} were studied at room temperature using X-ray diffraction (XRD) measurements at two beamlines BL15U1 (20 KeV, wavelength $\lambda = 0.6199$ Å) and BL14B1 (18 KeV, $\lambda = 0.6887$ Å) of the Shanghai Synchrotron Radiation Facility (SSRF), and the lattice parameters were obtained by lattice refinements, as

detailed in Subsections 2.3 and 2.4. At ambient pressure, the XRD results indicated that the NiTe_{2-x} single crystals were of high purity and demonstrated a pure hexagonal phase (H-phase) with $P\bar{3}m1$ symmetry. The lattice constants obtained from Rietveld refinements, $a = 3.8553$ Å and $c = 5.2630$ Å, were slightly smaller than those ($a = 3.8776$ Å, $c = 5.2653$ Å) found in nearly stoichiometric NiTe_{1.98} single crystals [28]. With increasing pressure, all diffraction peaks associated with the H-phase systematically moved towards higher angles, suggesting a steady decrease in the lattice constants, as shown in Fig. 1a and b. However, additional peaks associated with a monoclinic phase (M-phase) of P2/m symmetry emerged at a pressure between 14.51 GPa and 18.39 GPa, which coexisted with the H-phase and became more intense and also shifted towards higher angles with increasing pressure (Fig. 1a), implying decreasing lattice constants with pressure, as summarized in Fig. 1c. For detailed analysis of the crystalline structure, we show in Fig. 2a a representative synchrotron powder diffraction pattern at 23 GPa, where the newly emerged non-overlapped peaks at $2\theta = 10.422^\circ$, 14.957° and 17.320° can be well indexed by the M-phase of P2/m symmetry with $a = 3.4542$ Å, $b = 3.2362$ Å, $c = 4.8276$ Å and $\gamma = 94.0887^\circ$. Interestingly, the onset pressure for the emergence of the M-phase coincided with the Lifshitz transition in NiTe_{1.98} [28]. Additionally, the linewidths of the high-angle peaks associated with the H-phase appeared to broaden significantly with increasing pressure, particularly for the peaks at 2θ slightly below 25° , which differed from the sharp peaks found in NiTe_{1.98} [28]. The pressure-induced broadening of the linewidths at high angles may be attributed in part to more Bragg reflection peaks of the M-phase at higher diffraction angles, and also to the increasing lattice distortion between the newly emerged M-phase and the H-phase. A schematic illustration for the proposed structural evolution of the H- and M-phases with increasing

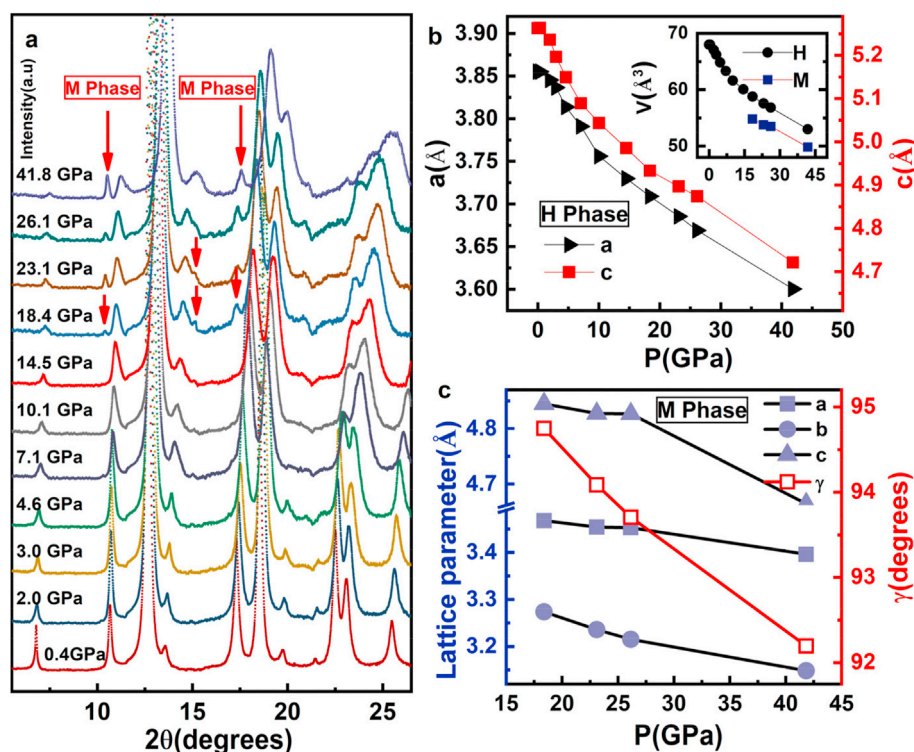


Fig. 1. XRD studies of the pressure-dependent lattice constants and crystalline symmetries of a NiTe_{2-x} ($x = 0.38 \pm 0.09$) single crystal: a, Evolution of the XRD peaks with pressure, where the primary set of peaks are associated with the hexagonal phase (H-phase) with $P\bar{3}m1$ symmetry, and a secondary set of peaks emerging at $P > 14.5$ GPa is associated with the monoclinic phase (M-phase) with P2/m symmetry; b, Pressure dependent lattice constants (a and c) of the H-phase; Inset, Pressure dependent unit volumes of the H- and M-phases; c, Pressure dependent lattice constants (a, b, c) and γ of the M-phase.

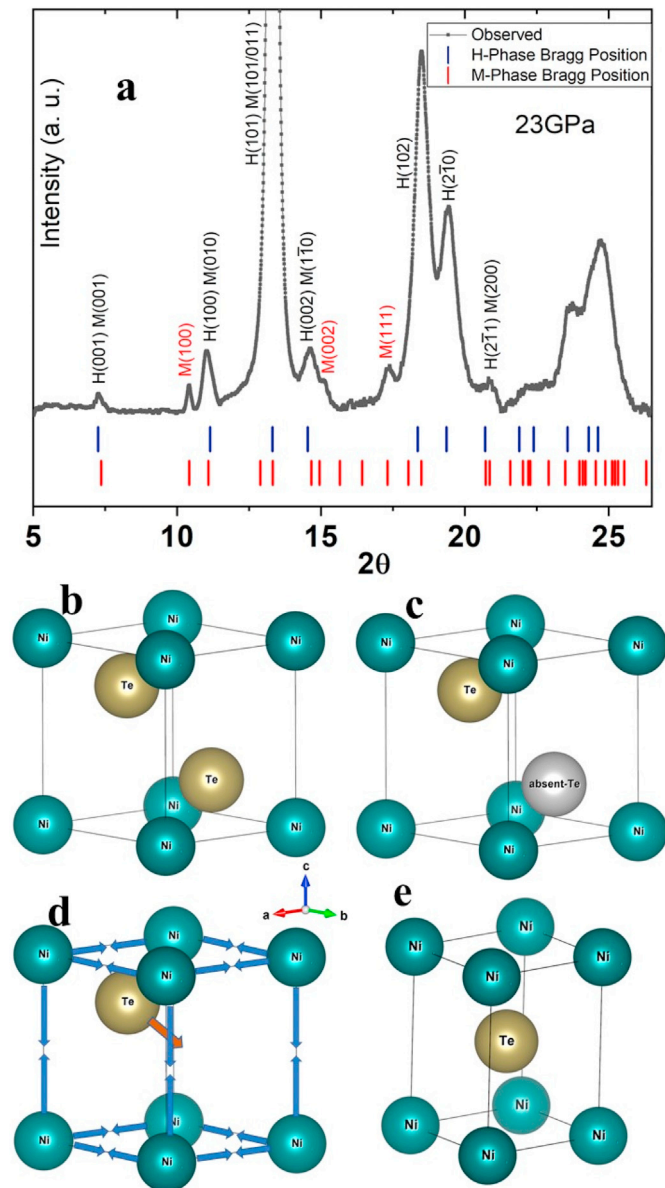


Fig. 2. a, Synchrotron powder diffraction pattern of NiTe_{2-x} taken at $P = 23$ GPa is shown to be well indexed by coexisting H- and M-phases, with two sets of Bragg reflection positions labeled under the diffraction pattern; b, c, d and e, Schematic illustrations for the proposed structural evolution of the H- and M-phases with increasing pressure in NiTe_{2-x} .

pressure in NiTe_{2-x} is shown in Fig. 2b–e. The Brillouin zones for the H- and M-phases with the corresponding high-symmetry points are illustrated in Figure S8.

4.2. Raman spectroscopic studies

To understand the effect of Te-vacancies on the pressure dependence of the phonon modes, we performed Raman spectroscopic studies of the E_g -mode associated with the in-plane Te vibrations (Fig. 3a), as detailed in Subsection 2.6. The E_g peaks were fit to the Lorentzian line shape, and the resulting peak positions and the full-width-half-maximum (FWHM) linewidths are shown in Figs. 3a and 5d, respectively. We found a steady increase in the frequency of the E_g -mode with pressure up to ~ 35 GPa, which was followed by a saturation at $P > 35$ GPa (Fig. 3b). The FWHM

linewidth exhibited an overall trend of increase with pressure, showing a smaller anomaly at $P \sim 16$ GPa and two larger anomalies at ~ 33 GPa and ~ 42 GPa (Fig. 5d). Noting that the pressure dependence of the peak position and the FWHM linewidth of NiTe_{2-x} for $P < 35$ GPa was consistent that of $\text{NiTe}_{1.98}$ [28], we may attribute the Raman peak in Fig. 3a to the in-plane Te-vibrational mode of the H-phase. On the other hand, the saturation of the Raman mode and the FWHM linewidth for $P > 35$ GPa may be associated with hybrid contributions from both the H- and the M-phase due to emergence of the latter above 35 GPa.

4.3. Electrical transport studies

To investigate the effect of pressure on the electrical transport properties and superconductivity of NiTe_{2-x} , we performed in-plane longitudinal resistance (R) and Hall coefficient (R_H) vs. temperature (T) measurements with the four-probe method for pressure up to 52.8 GPa, as described in Subsection 2.5. We found that the in-plane resistance of NiTe_{2-x} at ambient pressure was metallic, and became more conducting with increasing pressure as shown in Fig. 4, which was in stark contrast to the steady increase of resistance with pressure in $\text{NiTe}_{1.98}$ [28]. Additionally, superconductivity emerged at $P \sim 0.5$ GPa with a sharp onset transition temperature $T_{\text{SCI}}^{\text{onset}} = 3.4$ K (Fig. 4a). Both $T_{\text{SCI}}^{\text{onset}}$ and the zero resistance transition temperature $T_{\text{SCI}}^{\text{zero}}$ increased with pressure, reaching maxima $T_{\text{SCI}}^{\text{onset}} = 4.8$ K and $T_{\text{SCI}}^{\text{zero}} = 4.3$ K at 4.3 GPa (Fig. 4a). For $4.3 \text{ GPa} < P < 16$ GPa, both $T_{\text{SCI}}^{\text{onset}}$ and $T_{\text{SCI}}^{\text{zero}}$ gradually decreased with pressure (Fig. 4b), and then saturated at $T_{\text{SCI}}^{\text{onset}} = 2.8$ K and $T_{\text{SCI}}^{\text{zero}} = 2.2$ K over the pressure range $16 \text{ GPa} < P < 33$ GPa. Meanwhile, a second superconducting phase (SCII) appeared at $T_{\text{SCII}} = 6.0$ K for $P > 33$ GPa (Fig. 4c and d). The SCI and SCII phases coexisted for $33 \text{ GPa} < P < 47.3$ GPa, beyond which SCII took over and T_{SCII} reached a maximum value of ~ 7.8 K at 47.8 GPa, which remained nearly invariant for pressure up to 52.8 GPa. The overall pressure dependence of $T_{\text{SCI,SCII}}^{\text{onset}}$ and $T_{\text{SCI,SCII}}^{\text{zero}}$ is summarized in Fig. 5a.

The Hall coefficient (R_H) was obtained in the normal state at 10 K with the van der Pauw method by applying different external magnetic fields (B) perpendicular to the crystalline plane and measuring the resulting Hall resistivity ρ_{xy} so that $R_H = (\rho_{xy}/B)$. We found that R_H was negative at ambient pressure, suggesting predominant electron carriers due to Te-vacancies. With increasing pressure, however, R_H became positive for $P > 1.5$ GPa, with the sign change occurring slightly above the emergence of a finite $T_{\text{SCI}}^{\text{zero}}$, reaching a maximum at ~ 4.3 GPa where both $T_{\text{SCI}}^{\text{onset}}$ and $T_{\text{SCI}}^{\text{zero}}$ were also at the maximum (Fig. 5a and b). With further pressure increase, R_H intimately followed the pressure dependence of $T_{\text{SCI}}^{\text{onset}}$ and $T_{\text{SCI}}^{\text{zero}}$ so that R_H gradually decreased with pressure for $5 \text{ GPa} < P < 16$ GPa, reaching 0 at $P \sim 16$ GPa and remained nearly 0 up to 33 GPa, as shown in Fig. 5b. Interestingly, the resistance R ($T = 10 \text{ K}, P$) also remained nearly independent of pressure over the same pressure range where $R_H \sim 0$ (Fig. 5c). Eventually, R_H became negative when SCII superconductivity emerged above 33 GPa, and $|R_H|$ increased gradually with pressure and saturated when SCII dominated above 47.3 GPa (Fig. 5b).

The aforementioned R_H -vs.- P behavior in NiTe_{2-x} was drastically different from that in $\text{NiTe}_{1.98}$ [28]: The R_H values of $\text{NiTe}_{1.98}$ were positive for $0 < P < 15$ GPa, which steadily decreased with increasing pressure, reaching $R_H \sim 0$ at 16 GPa and becoming negative with its magnitude continuously increasing up to 78.2 GPa [28]. Such differences between the electrical transport properties of NiTe_{2-x} and $\text{NiTe}_{1.98}$ strongly suggest that Te-vacancies played a critical role in determining the normal-state electronic properties and the appearance of superconductivity in NiTe_{2-x} , as corroborated

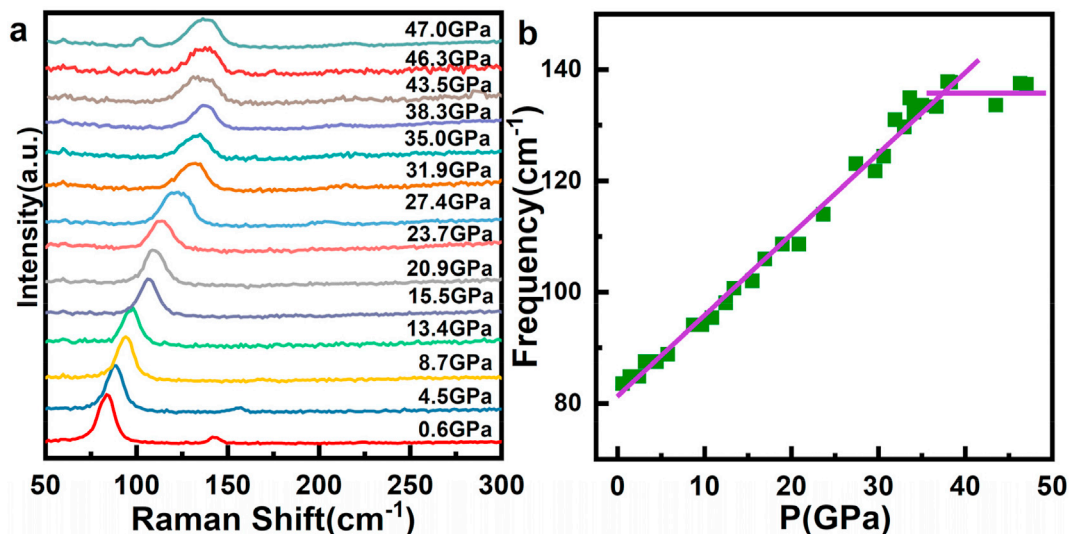


Fig. 3. Pressure-dependent Raman spectroscopic studies of NiTe_{2-x} : **a**, The E_g mode Raman spectra of NiTe_{2-x} under different pressure at room temperature; **b**, The evolution of E_g mode peak position with pressure, showing mostly monotonic increase of the frequency with pressure up to ~ 40 GPa where the frequency saturates. Here the peak position was obtained by fitting each spectrum to the Lorentzian line shape.

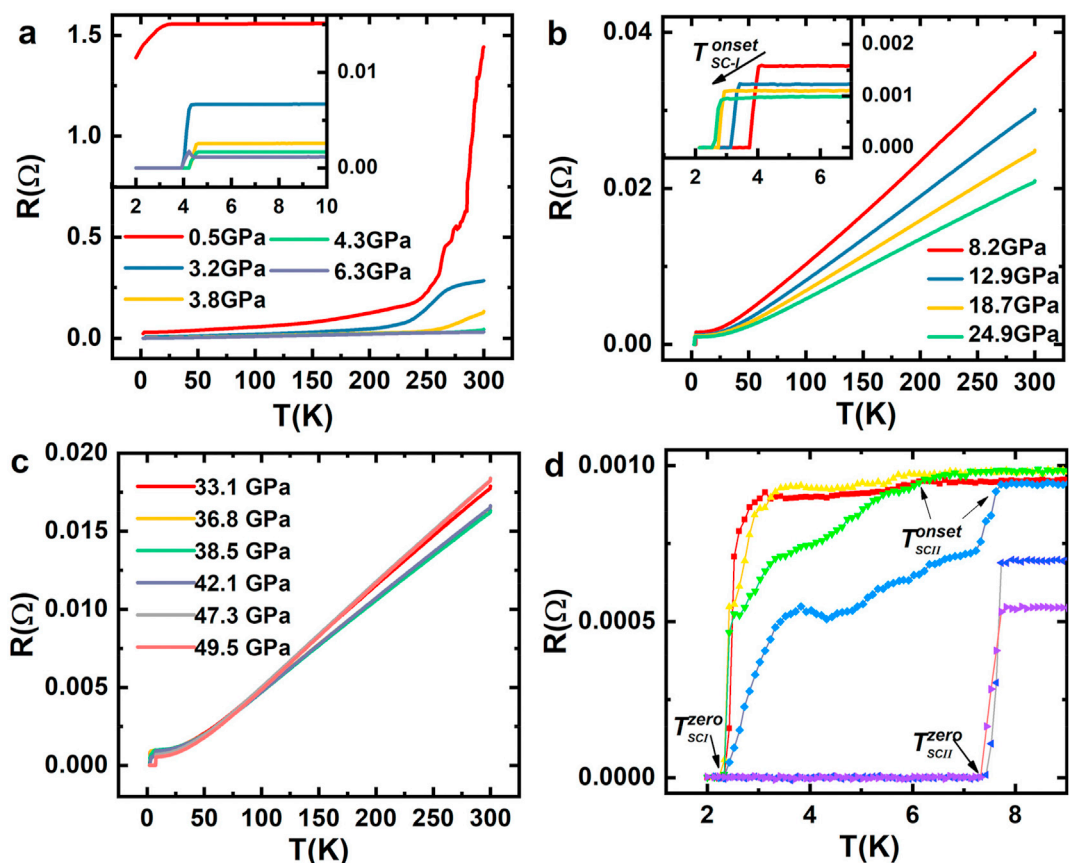


Fig. 4. Temperature-dependent longitudinal resistance $R(T, P)$ and superconducting transitions of single crystalline NiTe_{2-x} under different hydrostatic pressure (P): **a**, $R(T, P)$ -vs.- T curves for $0 < T < 300$ K (main panel) and $P = 1.0, 3.2, 3.8, 4.3$ and 6.3 GPa. The inset shows the same $R(T, P)$ -vs.- T curves for $2 \text{ K} \leq T \leq 20$ K. A superconducting phase SCI emerges at $P \geq 0.5$ GPa and the transition temperatures $T_{\text{SCI}}^{\text{zero}}$ and $T_{\text{SCI}}^{\text{onset}}$ both increase with increasing P . **b**, $R(T, P)$ -vs.- T curves for $0 < T < 300$ K (main panel) and $P = 8.1, 12.9, 18.7$ and 24.9 GPa. The inset shows the same $R(T, P)$ -vs.- T curves for $2 \text{ K} \leq T \leq 20$ K. The superconducting transition temperatures $T_{\text{SCI}}^{\text{zero}}$ and $T_{\text{SCI}}^{\text{onset}}$ both decrease with increasing P . **c**, $R(T, P)$ -vs.- T curves for $0 < T < 300$ K and $P = 33.1, 36.8, 38.5, 42.1, 47.3$ and 49.5 GPa. **d**, The same $R(T, P)$ -vs.- T curves as those shown in **c** and enlarged over the temperature interval $2 \text{ K} \leq T \leq 20$ K. $T_{\text{SCI}}^{\text{zero}}$ appears to saturate near 2.5 K and a second superconducting phase SCII with $T_{\text{SCII}}^{\text{onset}} \approx 6.0$ K emerges at $P > 33$ GPa. SCI and SCII coexist up to $P = 42.1$ GPa and then SCII takes over, with $T_{\text{SCII}}^{\text{onset}}$ increasing with P and reaching maximum $T_{\text{SCII}}^{\text{onset}} \approx 7.8$ K for $P = 49.5$ GPa.

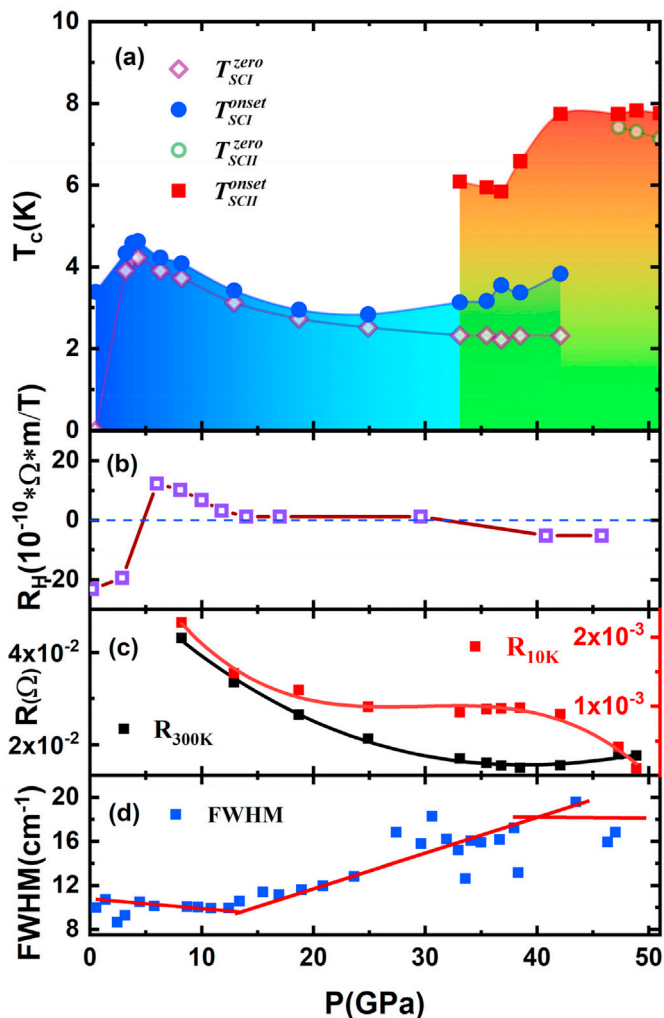


Fig. 5. Comparison of the pressure (P) dependence of various physical properties of NiTe_{2-x} ($x = 0.38 \pm 0.09$): **a**, Superconducting transition temperatures for SCI and SCII phases defined at the resistive transition onset ($T_{\text{SCI}}^{\text{onset}}$ and $T_{\text{SCII}}^{\text{onset}}$) and at zero resistance ($T_{\text{SCI}}^{\text{zero}}$ and $T_{\text{SCII}}^{\text{zero}}$). **b**, Hall coefficient R_H obtained in the normal state at $T = 10$ K and under an applied magnetic field $B = 100$ Oe along the sample c -axis. **c**, In-plane longitudinal resistance taken in zero magnetic fields at 10 K and 300 K. **d**, The FWHM linewidth of the E_g -mode as a function of pressure measured at 300 K, showing anomalies at ~ 16 GPa, ~ 33 GPa and ~ 42 GPa.

by our theoretical calculations of the ambient-pressure density of states (DOS) for NiTe_{1.625} and NiTe₂ (Figures S6c and S6d). Moreover, the pressure independence of the normal-state R_H and R as well as the superconducting transitions $T_{\text{SCI}}^{\text{onset}}$ and $T_{\text{SCI}}^{\text{zero}}$ over the pressure range of 16 GPa $< P < 33$ GPa implies a large degree of electronic degeneracies, which is consistent with the behavior of systems exhibiting non-trivial topological properties [20]. Additionally, this pressure range corresponds to the emergence of a globally connected M-phase within the H-phase matrix, which results in global inversion symmetry breaking and thus non-trivial Berry curvatures associated with the Dirac points near the Fermi level (see Figures S9a-b). The existence of a large degree of electronic degeneracy and non-trivial Berry curvatures suggests that it is promising to explore potential topological superconductivity in NiTe_{2-x}.

The upper critical fields $H_{c2}(T)$ of the two-phase superconductivity in NiTe_{2-x} were investigated by carrying out R -vs- T measurements in finite magnetic fields perpendicular to the basal planes of the single crystals. As shown in Fig. 6a–c for R -vs- T data

taken at different pressures and under different magnetic fields, the systematic left shift of the R -vs- T curves with increasing magnetic fields can be used to determine the $H_{c2}(T)$ values. Using the criterion $R(H = H_{c2}, T) \equiv 0.5 R(H = 0, T_c)$, we obtain the $H_{c2}(T)$ -vs- T curves for $P = 3.8$ GPa (SCI), 42.1 GPa (SCII) and 51.0 GPa (SCII) in Fig. 6d. The different curvatures of $H_{c2}(T)$ for the SCI and SCII phases are noteworthy. Specifically, the convex $H_{c2}(T)$ curves at $P = 42.1$ GPa and 51.0 GPa in the SCII phase (with $T_{\text{SCII}}^{\text{onset}} = 7.8$ K) appeared to be independent of pressure, and the T -dependence in the intermediate temperature range below $T_{\text{SCII}}^{\text{onset}}$ is consistent with the standard WHH-like shape for either single-band superconductivity [38] or for multiband/multilayer superconductors with orbitally-limited H_{c2} [39–42]. In contrast, the concave $H_{c2}(T)$ curve associated with the SCI phase has often been associated with either multi-band superconductors of novel interband pairing [39], such as in some iron-based superconductors [43,44]; or superconductors exhibiting the Fulde-Ferrel-Larkin-Ovchinnikov (FFLO) transition [45,46], such as in some heavy-fermion and organic superconductors [47–50].

To better understand the physical origin for the different H_{c2} behavior associated with the SCI and SCII phases, we carried out theoretical calculations for the DOS and bandstructures associated with the H-phase NiTe₂ and M-phase NiTe (see Figures S6–S10 and Section 3). We found that the DOS and bandstructures near the Fermi level E_F (the zero energy point) of the H-phase consisted of contributions from multiple Ni 3d-bands and Te 5p-bands so that the SCI phase was consistent with multi-band superconductivity (Figures S7a–c, S9a, S10a–b). In contrast, the DOS and bandstructures of the M-phase near E_F appeared to be dominated by a Ni 3d-band under high pressures (Figures S6a–b, S9b), suggesting a feasible single-band model for the SCII phase.

In addition to the aforementioned different H_{c2} behavior associated with the SCI and SCII phases, we note that the upper critical fields are relatively low in comparison with those of most superconductors of comparable T_c values. We speculate that field-induced magnetic order associated with the Ni ions may be the cause because the resulting finite magnetization would compete with the supercurrent-induced diamagnetism. Although in principle this conjecture may be verified by magnetization measurements of NiTe_{2-x} under high pressure, our current magnetometer cannot accommodate the size of the diamond anvil cell. Therefore, the possibility of field-induced magnetic order and the physical origin for the relatively low upper critical fields in NiTe_{2-x} remain open issues for future investigation.

5. Discussions

We conjecture the following scenario in an attempt to account for various novel experimental findings in the Te-deficient NiTe_{2-x}: At ambient pressure, our bandstructure and DOS calculations reveal that in the presence of Te-vacancies, excess electron carriers from Ni result in dominant Ni-3d DOS near E_F (Figure S6c) and therefore $R_H < 0$ (Figure S9a). With increasing pressure, sample regions containing Te-vacancies (Fig. 2d) begin to form small NiTe clusters (Fig. 2e) while the volume fraction of stoichiometric NiTe₂ (Fig. 2b) increases upon the release of Te-vacancies, leading to dominant hole carriers (Figure S9a) associated with the majority H-phase [28] up to ~ 4.5 GPa. Further pressure increase results in larger NiTe clusters as well as the downturn of R_H due to rapidly decreasing R_H found in NiTe_{1.98} [28]. The transformation of Te-vacancy sites in the H-phase (Fig. 2d) into NiTe clusters continues for 4.5 GPa $< P < P_c \sim 16$ GPa, and the clusters become globally connected into the M-phase at P_c so that the corresponding XRD peaks emerge (Fig. 1a), and the XRD peaks associated with the H-phase

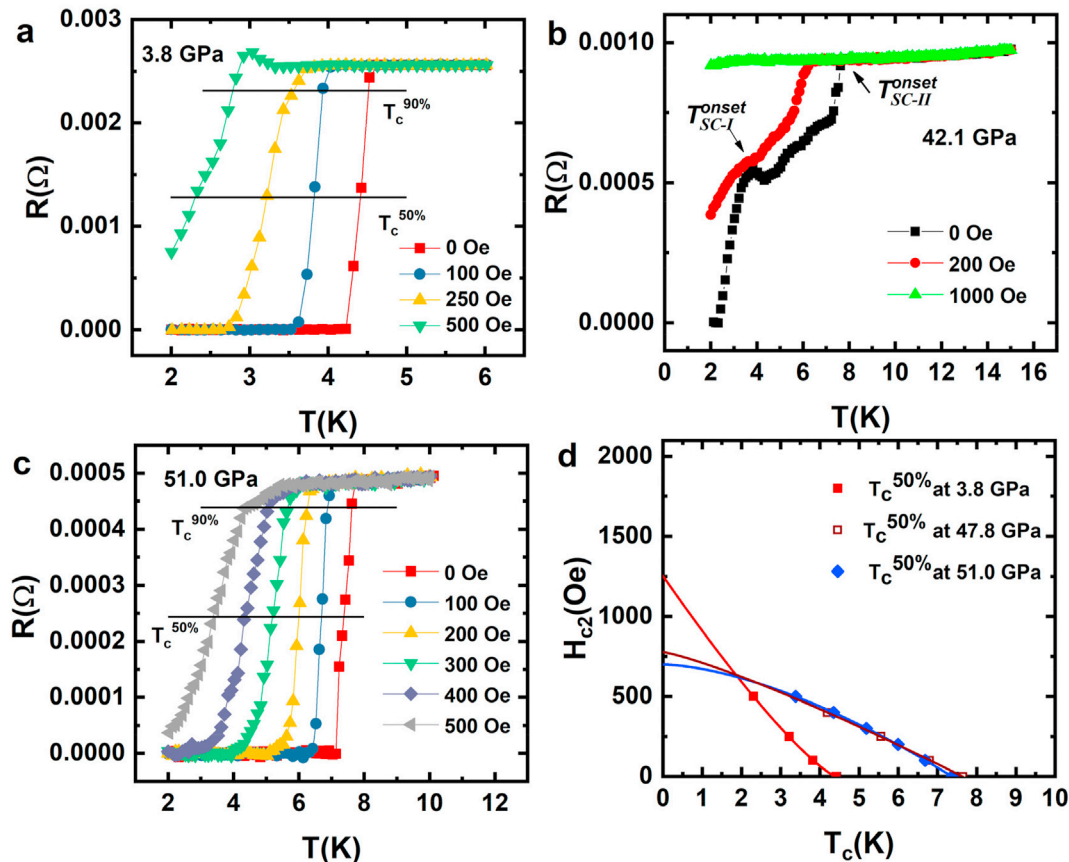


Fig. 6. Studies of the upper critical fields of NiTe_{2-x} superconductors: **a**, Resistance (R) vs. temperature (T) measurements taken with $P = 3.8$ GPa and under different c -axis magnetic fields $H = 0, 100$ Oe, 250 Oe and 500 Oe; **b**, R -vs.- T measurements taken with $P = 42.1$ GPa and under c -axis magnetic fields $H = 0, 200$ Oe and 1000 Oe; **c**, R -vs.- T measurements taken with $P = 51$ GPa and under c -axis magnetic fields $H = 0, 100$ Oe, 200 Oe, 300 Oe, 400 Oe, and 500 Oe; **d**, Upper critical fields $H_{c2}(T)$ determined by the criterion of 50% normal-state resistance taken with $P = 3.8$ GPa (SCI), 47.8 GPa (SCII) and 51 GPa (SCII), showing concave $H_{c2}(T)$ behavior for the SCI phase and convex and pressure independent $H_{c2}(T)$ behavior for the SCII phase.

around $2\theta = 22.5^\circ$ begin to broaden significantly. Meanwhile, R_H follows the same decreasing trend towards 0 for 4.5 GPa $< P < P_c$ as that in NiTe_{1.98} [28] before the M-phase emerges. For $P_c < P < 33$ GPa, the crystalline M-phase with strongly enhanced DOS near E_F (Figures S6a-b) appears to have an overall charge compensation effect on the H-phase so that R_H remains 0 instead of continuously decreasing to negative values as in NiTe_{1.98} [28]. The physical mechanism for this interesting charge compensation effect is currently unknown and will require future investigation. Above 33 GPa, the transformation of Te-vacancy sites into the M-phase becomes mostly complete while the R_H value associated with the H-phase continues to decrease, leading to $R_H < 0$ and the onset of SCII superconductivity. Further increase of pressure above 42.1 GPa leads to dominance of the SCII phase and strong hybridization of the H- and M-phases due to compression of both phases into similar volumes (inset of Fig. 1b), suggesting that SCII is primarily associated with a hybridized structure with dominant electron carriers.

In contrast, the small concentration of Te-vacancies in NiTe_{1.98} cannot lead to the formation of a globally connected M-phase in the high-pressure limit. Consequently, increasing pressure only leads to steady reduction of the lattice constants of the H-phase [28] and suppression of DOS near E_F (Figures S10a-b), leading to steady increase of resistance with pressure in NiTe_{1.98} [28]. We further note that the range of pressure-dependent changes in R_H is more than one order of magnitude different between NiTe_{2-x} and NiTe_{1.98}: For NiTe_{1.98}, the range of R_H is from $\sim +1 \times 10^{-10}$ Ω m/T to $\sim -$

1×10^{-10} Ω m/T for $P = 0-71.2$ GPa. In contrast, the range of R_H for NiTe_{2-x} varies from $\sim -22 \times 10^{-10}$ Ω m/T to $\sim +12 \times 10^{-10}$ Ω m/T for $P = 0-52.8$ GPa. Additionally, theoretical calculations of the electronic bandstructures and DOS of the M-phase revealed significant differences from those of the H-phase (Figures S6-S10). In particular, a strong DOS peak is found to move from $E \leq -2$ eV in the H-phase to $E \sim -1$ eV in the M-phase (Figures S6a-b, S7a-c), and the enhanced DOS near E_F in the M-phase (Figures S6a-b) may be relevant to the occurrence of superconductivity. We further note that the Dirac point at $E \sim -0.17$ eV along Γ -A in the H-phase at $P = 0$ (Figure S9a) becomes lifted for $P > P_c$ (Figures S10a-b), whereas a new Dirac point appears in the M-phase along A-X at $E \sim 0.17$ eV (Figure S9b).

Finally, we note that the pressure-induced superconductivity in NiTe_{2-x} ($x = 0.38 \pm 0.09$) first emerges at a relatively low pressure of 0.5 GPa, reaching maximum $T_c \sim 7.8$ K at 47.8 GPa and persisting up to 52.8 GPa. This behavior differs from the typical dome-like T_c -vs.- P behavior in most pressure-induced superconductivity and is similar to recent findings of T_c resurgence in cuprate superconductors due to pressure-induced electronic transitions [51]. Additionally, the low pressure for inducing superconductivity in NiTe_{2-x} suggests that ambient-pressure superconductivity may be achieved by optimizing the Ni-to-Te ratio in bulk NiTe_{2-x} or by engineering the strain in NiTe_{2-x} epitaxial thin films. Recent observation of ambient-pressure hole-type superconductivity in Ni_{1-x}Re_xTe₂ single crystals (with $T_c = 2.3$ K and 2.4 K for $x = 0.1$ and 0.2, respectively) [52] is consistent with the notation that proper doping and significant

lattice distortion induced by either external or chemical pressure in NiTe_{2-x} can lead to ambient-pressure superconductivity.

6. Conclusion

In conclusion, we present in this work experimental evidences for pressure-induced two-phase (SCI and SCII) superconductivity with a maximum $T_c = 7.8$ K as well as pressure-induced mixed structures of NiTe_2 and NiTe in bulk NiTe_{2-x} single crystals ($x = 0.38 \pm 0.09$) from measurements of synchrotron XRD, Raman spectroscopy, resistivity, Hall coefficients and upper critical fields from ambient pressure to 52.8 GPa. Detailed analyses suggest that the SCI phase is associated with the hole-dominant ($\text{NiTe}_2 + \text{Te}$ -vacancies) phase of the $\text{P}\bar{3}m1$ symmetry, whereas the SCII phase is primarily related to the electron-dominant NiTe phase of the $\text{P}2/m$ symmetry (M-phase) hybridized with the H-phase in the high pressure limit (> 33 GPa). The different temperature dependence of the upper critical fields for SCI and SCII phases together with theoretical DOS and bandstructure calculations further suggest that the formal is consistent with multi-band superconductivity and the latter with single-band superconductivity. Additionally, the Dirac point closest to the Fermi level (E_F) of NiTe_{2-x} is found to shift with pressure from below E_F in the H-phase to above E_F in the M-phase. Our discovery of pressure-induced two-phase superconductivity in non-stoichiometric NiTe_{2-x} single crystals is significant because it differs fundamentally from the theoretically predicted absence of superconductivity in bulk stoichiometric NiTe_2 , and therefore suggests a pathway towards modifying TMDs by introducing vacancies and pressure to achieve new structural and electronic phases. Moreover, the finding of several physical quantities (e.g., R_H , R and T_c) invariant over a wide range of pressure where the M-phase becomes globally connected within the H-phase matrix implies that a large degree of electronic degeneracy and finite Berry curvatures exist in the SCI phase of NiTe_{2-x} , which is promising for further investigation of potential topological superconductivity.

Credit author statement

Zhenjie Feng, Supervision, Conceptualization, Formal analysis, Investigation, Writing – review & editing, Visualization, Project administration, Funding acquisition. Jingying Si, Tao Li, Investigation, Visualization, Formal analysis, Writing – original draft. Hongliang Dong, Ke Wang, Hao Wu, Qiang Hou, Juanjuan Xing, Shun Wan, Shujia Li, Wen Deng, Jiajia Feng, Arnab Pal, Fei Chen, Jun-Yi Ge, Shenghao Wang, Data curation, Validation. Chunqiang Xu, Yi Liu, Xiaofeng Xu, Resources. Jiong Yang, Zhou Zhang, Shunbo Hu, Formal analysis, Software, Visualization. Cheng Dong, Wei Ren, Shixun Cao, Formal analysis. Jincang Zhang, Bin Chen, Funding acquisition, Project administration. Nai-Chang Yeh, Formal analysis, Investigation, Writing – review & editing, Project administration, Funding acquisition.

Declaration of competing interest

The authors declare that they have no known competing financial interests or personal relationships that could have appeared to influence the work reported in this paper.

Acknowledgements

This work at the Shanghai University (SHU) is jointly supported by the Ministry of Science and Technology of the People's Republic of China No. (2020YFB0704503, 2016YFB0700201, 2018YFB0704400), National Natural Science Foundation of China

(11774217, 11974061, U1732162, 10904088), Shanghai Pujiang Program (13PJD015), and Science and Technology commission of Shanghai Municipality (13ZR1415200). The research at the California Institute of Technology was supported by the National Science Foundation under the Institute for Quantum Information and Matter (award #1733907). N.-C. Yeh acknowledges the hospitality and sponsorship of her visit to the SHU under the Overseas Expert Recruitment Program at SHU. The authors thank both BL15U1 and BL14B1 beamlines at the SSRF for providing the beam time, and also thank Professor Patrick A. Lee from Massachusetts Institute of Technology for stimulating discussions.

Appendix A. Supplementary data

Supplementary data to this article can be found online at <https://doi.org/10.1016/j.mtphys.2020.100339>.

References

- [1] K.S. Novoselov, A. Mishchenko, A. Carvalho, A.H.C. Neto, 2D materials and van der Waals heterostructures, *Science* 353 (2016) 9439.
- [2] S. Manzeli, D. Ovchinnikov, D. Pasquier, O.V. Yazyev, A. Kis, 2D transition metal dichalcogenides, *Nat. Rev. Mater.* 2 (2017) 1–15.
- [3] Y.-Y. Lv, X. Li, B.-B. Zhang, W.Y. Deng, S.-H. Yao, Y.B. Chen, J. Zhou, S.-T. Zhang, M.-H. Lu, L. Zhang, M. Tian, L. Sheng, Y.-F. Chen, Experimental observation of anisotropic adler-bell-jackiw anomaly in type-II Weyl semimetal $\text{WTe}_{1.98}$ crystals at the quasiclassical regime, *Phys. Rev. Lett.* 118 (2017): 096603.
- [4] M. Udagawa, E.J. Bergholtz, Field-selective anomaly and chiral mode reversal in type-II Weyl materials, *Phys. Rev. Lett.* 117 (2016): 086401.
- [5] J.M. Lu, O. Zheiliuk, I. Leermakers, N.F.Q. Yuan, U. Zeitler, K.T. Law, J.T. Ye, Evidence for two-dimensional Ising superconductivity in gated MoS_2 , *Science* 350 (2015) 1353–1357.
- [6] E. Sohn, X. Xi, W.-Y. He, S. Jiang, Z. Wang, K. Kang, J.-H. Park, H. Berger, L. Forro, M.T. Hwang, K.F. Mak, L. Sheng, Y.-F. Chen, Unusual continuous paramagnetic-limited superconducting phase transition in 2D NbSe_2 , *Nat. Mater.* 17 (2018) 504–508.
- [7] W.-Y. He, B.T. Zhou, J.J. He, N.F.Q. Yuan, T. Zhang, K.T. Law, Magnetic field driven nodal topological superconductivity in monolayer transition metal dichalcogenides, *Commun. Phys.* 1 (2018) 40.
- [8] Y. Qi, P.G. Naumov, M.N. Ali, C.R. Rajamathi, W. Schnelle, O. Barkalov, M. Hanfland, S.-C. Wu, C. Shekhar, Y. Sun, V. Süß, M. Schmidt, U. Schwarz, E. Pippel, P. Werner, R. Hillebrand, T. Förster, E. Kampert, S. Parkin, R.J. Cava, C. Felser, B. Yan, S.A. Medvedev, Superconductivity in Weyl semimetal candidate MoTe_2 , *Nat. Commun.* 7 (2016) 11038.
- [9] D. Kang, Y. Zhou, W. Yi, C. Yang, J. Guo, Y. Shi, S. Zhang, Z. Wang, C. Zhang, S. Jiang, A. Li, K. Yang, Q. Wu, G. Zhang, L. Sun, Z. Zhao, Superconductivity emerging from a suppressed large magnetoresistant state in tungsten ditelluride, *Nat. Commun.* 6 (2015) 7804.
- [10] X.-C. Pan, X. Chen, H. Liu, Y. Feng, Z. Wei, Y. Zhou, Z. Chi, L. Pi, F. Yen, F. Song, X. Wan, Z. Yang, B. Wang, G. Wang, Y. Zhang, Pressure-driven dome-shaped superconductivity and electronic structural evolution in tungsten ditelluride, *Nat. Commun.* 6 (2015) 7805.
- [11] F.C. Chen, X. Luo, R.C. Xiao, W.J. Lu, B. Zhang, H.X. Yang, J.Q. Li, Q.L. Pei, D.F. Shao, R.R. Zhang, L.S. Ling, C.Y. Xi, W.H. Song, Y.P. Sun, Superconductivity enhancement in the S-doped Weyl semimetal candidate MoTe_2 , *Appl. Phys. Lett.* 108 (2016) 162601.
- [12] H. Takahashi, T. Akiba, K. Imura, T. Shiino, K. Deguchi, N.K. Sato, H. Sakai, M.S. Bahramy, S. Ishiwata, Anticorrelation between polar lattice instability and superconductivity in the Weyl semimetal candidate MoTe_2 , *Phys. Rev. B* 95 (2017) 100501.
- [13] R. Dahal, L.Z. Deng, N. Poudel, M. Gooch, Z. Wu, H.C. Wu, H.D. Yang, C.K. Chang, C.W. Chu, Tunable structural phase transition and superconductivity in the Weyl semimetal $\text{Mo}_{1-x}\text{W}_x\text{Te}_2$, *Phys. Rev. B* 101 (2020) 140505.
- [14] L. Zhu, Q.-Y. Li, Y.-Y. Lv, S. Li, X.-Y. Zhu, Z.-Y. Jia, Y.B. Chen, J. Wen, S.-C. Li, Superconductivity in potassium-intercalated td-WTe_2 , *Nano Lett.* 18 (2018) 6585–6590.
- [15] A.J.S. Machado, N.P. Baptista, B.S. de Lima, N. Chaia, T.W. Grant, L.E. Correa, S.T. Renosto, A.C. Scaramussa, R.F. Jardim, M.S. Torikachvili, J. Albino Aguiar, O.C. Cigarroa, L.T.F. Eleno, Z. Fisk, Evidence for topological behavior in superconducting $\text{Cu}_x\text{ZrTe}_{2-y}$, *Phys. Rev. B* 95 (2017) 144505.
- [16] H.-j. Noh, J. Jeong, E.-J. Cho, K. Kim, B.I. Min, B.-G. Park, Experimental realization of type-II Dirac fermions in a PdTe_2 superconductor, *Phys. Rev. Lett.* 119 (2017): 16401.
- [17] M. Yan, H. Huang, K. Zhang, E. Wang, W. Yao, K. Deng, G. Wan, H. Zhang, M. Arita, H. Yang, Z. Sun, H. Yao, Y. Wu, S. Fan, W. Duan, S. Zhou, Lorentz-violating type-II Dirac fermions in transition metal dichalcogenide PtTe_2 , *Nat. Commun.* 8 (2017) 257.
- [18] M. Ettenberg, K.L. Komarek, E. Miller, Thermodynamic properties of nickel-tellurium alloys, *J. Solid State Chem.* 1 (1970) 583–592.

- [19] W. Bensch, W. Heid, M. Muhler, S. Jobic, R. Brec, J. Rouxel, Anionic polymeric bonds in nickel ditelluride: crystal structure, and experimental and theoretical band structure, *J. Solid State Chem.* 121 (1996) 87–94.
- [20] C. Xu, B. Li, W. Jiao, W. Zhou, B. Qian, R. Sankar, N.D. Zhigadlo, Y. Qi, D. Qian, F.-C. Chou, X. Xu, Topological type-II Dirac fermions approaching the Fermi level in a transition metal dichalcogenide NiTe₂, *Chem. Mater.* 30 (2018) 4823–4830.
- [21] C.M. Wang, H.-Z. Lu, S.-Q. Shen, Anomalous phase shift of quantum oscillations in 3D topological semimetals, *Phys. Rev. Lett.* 117 (2016): 077201.
- [22] Q. Liu, F. Fei, B. Chen, X. Bo, B. Wei, S. Zhang, M. Zhang, F. Xie, M. Naveed, X. Wan, F. Song, B. Wang, Nontopological origin of the planar Hall effect in the type-II Dirac semimetal NiTe₂, *Phys. Rev. B* 99 (2019) 155119.
- [23] F. Zheng, X.-B. Li, Y. Lin, L. Xiong, X. Chen, J. Feng, Emergent superconductivity in two-dimensional NiTe₂ crystals, *Phys. Rev. B* 101 (2020) 100505.
- [24] K. Kirshenbaum, P.S. Syers, A.P. Hope, N.P. Butch, J.R. Jeffries, S.T. Weir, J.J. Hamlin, M.B. Maple, Y.K. Vohra, J. Paglione, Pressure-induced unconventional superconducting phase in the topological insulator Bi₂Se₃, *Phys. Rev. Lett.* 111 (2013): 087001.
- [25] L. He, Y. Jia, S. Zhang, X. Hong, C. Jin, S. Li, Pressure-induced superconductivity in the three-dimensional topological Dirac semimetal Cd₃As₂, *Npj Quantum Mater* 1 (2016) 16014.
- [26] Y. Li, Y. Zhou, Z. Guo, F. Han, X. Chen, P. Lu, X. Wang, C. An, Y. Zhou, J. Xing, G. Du, X. Zhu, H. Yang, J. Sun, Z. Yang, W. Yang, H.-K. Mao, Y. Zhang, H.-H. Wen, Concurrence of superconductivity and structure transition in Weyl semimetal TaP under pressure, *Npj Quantum Mater* 2 (2017) 66.
- [27] A.F. Kusmartseva, B. Sipos, H. Berger, L. Forro, E. Tutis, Pressure induced superconductivity in pristine 1T-TiSe₂, *Phys. Rev. Lett.* 103 (2009) 236401.
- [28] M. Qi, C. An, Y. Zhou, H. Wu, B. Zhang, C. Chen, Y. Yuan, S. Wang, Y. Zhou, X. Chen, R. Zhang, Z. Yang, Pressure-driven Lifshitz transition in type-II Dirac semimetal InTe₂, *Phys. Rev. B* 101 (2020) 115124.
- [29] B.H. Toby, R.B. Von Dreele, GSAS-II: the genesis of a modern open-source all purpose crystallography software package, *J. Appl. Crystallogr.* 46 (2013) 544–549.
- [30] C. Prescher, V.B. Prakapenka, DIOPTAS: a program for reduction of two-dimensional X-ray diffraction data and data exploration, *High Pres. Res.* 35 (2015) 223–230.
- [31] A. Altomare, C. Cuocci, C. Giacovazzo, A. Moliterni, R. Rizzi, N. Corriero, A. Falcicchio, EXPO2013: a kit of tools for phasing crystal structures from powder data, *J. Appl. Crystallogr.* 46 (2013) 1231–1235.
- [32] J. Rodríguez-Carvajal, Recent advances in magnetic structure determination by neutron powder diffraction, *Phys. B Condens. Matter* 192 (1993) 55–69.
- [33] K. Momma, F. Izumi, VESTA 3 for Three-Dimensional Visualization of Crystal, Volumetric and Morphology Data, 2011.
- [34] G. Kresse, J. Furthmüller, Efficient iterative schemes for ab initio total-energy calculations using a plane-wave basis set, *Phys. Rev. B* 54 (1996) 11169–11186.
- [35] J.P. Perdew, K. Burke, M. Ernzerhof, Generalized gradient approximation made simple, *Phys. Rev. Lett.* 77 (1996) 3865–3868.
- [36] G. Kresse, D. Joubert, From ultrasoft pseudopotentials to the projector augmented-wave method, *Phys. Rev. B* 59 (1999) 1758–1775.
- [37] A. Zunger, S.-H. Wei, L.G. Ferreira, J.E. Bernard, Special quasirandom structures, *Phys. Rev. Lett.* 65 (1990) 353–356.
- [38] N.R. Werthamer, E. Helfand, P.C. Hohenberg, Temperature and purity dependence of the superconducting critical field, H_{c2}. III. Electron spin and spin-orbit effects, *Phys. Rev.* 147 (1966) 295–302.
- [39] A. Gurevich, Upper critical field and the Fulde-Ferrell-Larkin-Ovchinnikov transition in multiband superconductors, *Phys. Rev. B* 82 (2010) 184504.
- [40] R.A. Klemm, A. Luther, M.R. Beasley, Theory of the upper critical field in layered superconductors, *Phys. Rev. B* 12 (1975) 877–891.
- [41] S. Takahashi, M. Tachiki, Theory of the upper critical field of superconducting superlattices, *Phys. Rev. B* 33 (1986) 4620–4631.
- [42] S. Takahashi, M. Tachiki, New phase diagram in superconducting superlattices, *Phys. Rev. B* 34 (1986) 3162–3164.
- [43] G. Fuchs, S.-L. Drechsler, N. Kozlova, G. Behr, A. Köhler, J. Werner, K. Nenkov, R. Klingeler, J. Hamann-Borrero, C. Hess, A. Kondrat, M. Grobosch, A. Narduzzo, M. Knupfer, J. Freudenberger, B. Büchner, L. Schultz, High-field pauli-limiting behavior and strongly enhanced upper critical magnetic fields near the transition temperature of an arsenic-deficient La_{0.9}F_{0.1}FeAs_{1-δ} superconductor, *Phys. Rev. Lett.* 101 (2008) 237003.
- [44] M.M. Altarawneh, K. Collar, C.H. Mielke, N. Ni, S.L. Bud'ko, P.C. Canfield, Determination of anisotropic H_{c2} up to 60 T in Ba_{0.55}K_{0.45}Fe₂As₂ single crystals, *Phys. Rev. B* 78 (2008) 220505.
- [45] P. Fulde, R.A. Ferrell, Superconductivity in a strong spin-exchange field, *Phys. Rev.* 135 (1964) A550–A563.
- [46] A.I. Larkin, Yun. Ovchinnikov, Nonuniform state of superconductors, *Sov. Phys. - JETP* 20 (1965).
- [47] A. Bianchi, R. Movshovich, C. Capan, P.G. Pagliuso, J.L. Sarrao, Possible fulde-ferrell-larkin-ovchinnikov superconducting state in CeCoIn₅, *Phys. Rev. Lett.* 91 (2003) 187004.
- [48] M. Kenzelmann, T. Strässle, C. Niedermayer, M. Sigrist, B. Padmanabhan, M. Zolliker, A.D. Bianchi, R. Movshovich, E.D. Bauer, J.L. Sarrao, J.D. Thompson, Coupled superconducting and magnetic order in CeCoIn₅, *Science* 321 (2008) 1652–1654.
- [49] S. Uji, T. Terashima, M. Nishimura, Y. Takahide, T. Konoike, K. Enomoto, H. Cui, H. Kobayashi, A. Kobayashi, H. Tanaka, M. Tokumoto, E.S. Choi, T. Tokumoto, D. Graf, J.S. Brooks, Vortex dynamics and the Fulde-Ferrell-Larkin-Ovchinnikov state in a magnetic-field-induced organic superconductor, *Phys. Rev. Lett.* 97 (2006) 157001.
- [50] R. Lortz, Y. Wang, A. Demuer, P.H.M. Boettger, B. Bergk, G. Zwirnagl, Y. Nakazawa, J. Wosnitza, Calorimetric evidence for a Fulde-Ferrell-Larkin-Ovchinnikov superconducting state in the layered organic superconductor κ-(BEDT-TTF)₂Cu(NCS)₂, *Phys. Rev. Lett.* 99 (2007) 187002.
- [51] L. Deng, Y. Zheng, Z. Wu, S. Huyan, H.-C. Wu, Y. Nie, K. Cho, C.-W. Chu, Higher superconducting transition temperature by breaking the universal pressure relation, *Proc. Natl. Acad. Sci. Unit. States Am.* 116 (2019) 2004–2008.
- [52] M. Mandal, R.P. Singh, Emergent Superconductivity by Re Doping in Type -II Weyl Semimetal NiTe₂, 2020. ArXiv:2009.08690 [Cond-Mat].